Cavity soliton inhibition of extreme events in lasers with injection

M. Eslami,[1] E. Taati,[2] R. Kheradmand,[2] F. Prati,[3] G. Tissoni,[4] and G.-L. Oppo[5]

[1] Department of Physics, University of Guilan, P.O. Box 41335-1914 Rasht, Iran

[2] Faculty of Physics, University of Tabriz, 5166616471 Tabriz, Iran

[3] Dipartimento di Scienza e Alta Tecnologia, Università dell'Insubria, Via Valleggio 11, IT-22100 Como, Italy

[4] Université Côte d'Azur, CNRS, Institut de Physique de Nice, 1361 Route des Lucioles, FR-06560 Valbonne, France

[5] SUPA and Department of Physics, University of Strathclyde, Glasgow, G4 0NG, Scotland, UK

(*Electronic mail: meslami.ac@gmail.com)

(Dated: 22 April 2024)

Vortex mediated turbulence can be the key element in the generation of extreme events in spatially extended lasers with optical injection. Here we study the interplay of vortex mediated turbulence and cavity solitons on the onset of extreme events in semiconductor lasers with injection. We first analyse and characterise these two features separately, spatio-temporal chaotic optical vortices for low values of the injection intensity and cavity solitons above the locking regime. In regimes where vortex mediated turbulence and cavity solitons coexist, localized peaks of light inhibit instead of enhance the generation of rogue waves by locally regularising the otherwise chaotic phase of the optical field. Cavity solitons can then be used to manipulate and control extreme events in systems displaying vortex mediated turbulence.

The connection between cavity solitons and rogue waves in lasers is a complex interplay that has significant implications for the dynamics of optical systems. On the other hand, the presence of vortex mediated turbulence in the laser systems with injection has been identified as a key mechanism for the generation of rogue waves. When both features are present, the cavity solitons are observed to inhibit the generation of rogue waves by imposing order on the chaotic phase of the optical field. This intricate interaction highlights the potential for cavity solitons to locally control extreme events in laser systems, offering opportunities for enhanced stability and control in applications such as imaging and sensing.

I. INTRODUCTION

Oceanic rogue waves (RWs) found their optical counterparts by the first observation of extreme events in a physical system based on a microstructured optical fiber[1]. Since then, the topic has been the focus of research in many optical systems and has led to remarkable advances in understating their basic concepts and underlying mechanisms[2–7].

One peculiar mechanism for the generation of optical RWs in spatially extended lasers and optical parametric oscillators has been identified in 2016 via vortex mediated turbulence (VMT) and interacting defects[8] with obvious connections to hydrodynamics[9]. Since then several other mechanisms for spatio-temporal RWs in optical systems with large aspect ratio have been described in the literature such as nonlinear spatio-temporal instabilities and bifurcations[10–14], competition of patterns[15], and cavity solitons (CSs)[16].

Although RWs are known for their sudden, unpredictable and uncontrollable occurrences, recent techniques proposed for their prediction and control have added to the feasibility of their potential applications[17–21]. Imaging and sensing tech-

nologies, for example, can benefit from the generation of high-amplitude optical pulses to improve image quality via enhanced signal-to-noise ratio or sensitivity through increased output-to-input change ratio. In this respect, spatially extended semiconductor lasers, such as vertical-cavity surface-emitting lasers (VCSELs), are suitable candidates to be studied due to their unique features such as compactness, ease of integration on various optical devices, and advanced fabrication technologies[22,23]. Two-dimensional RWs have recently been investigated in broad-area semiconductor lasers in a variety of configurations, see for instance[11,12,16,21,24] for those with a saturable absorber,[20] for those with delayed-feedback and[25] for those with coherent injection.

The RW mechanism through VMT described in[9,26] is universal in nonlinear optics and has been recently extended to models of coherently injected broad-area VCSELs that include the linewidth enhancement factor α and retains carrier density dynamics[25]. Below the injection locking point the lower branch of the homogeneous stationary state (HSS) is Hopf unstable[27] and is prone to exhibit spatio-temporal chaotic structures. Investigation of the chaotic dynamics of our system below the injection locking threshold (Hopf instability region) reveals that the amplitude of the oscillations increases with the reduction of the injection intensity leading to large densities of vortex singularities where the carrier density is high. In agreement with[9], it is close to these singularities that we observe the appearance of rogue waves.

In[25] the polarization of the semiconductor medium was adiabatically eliminated and a reduced form of Maxwell-Bloch equations with an added diffusive term[28] was employed to successfully describe RW formation. It speeds up the computations but requires a careful determination of the diffusive term[28]. We consider here the full set of Maxwell-Bloch equations to describe a broad-area VCSEL above laser threshold, driven by an external coherent beam and displaying CSs[29–31]. CSs have been reported to exist below the injection locking threshold and atop a spatio-temporally unstable background
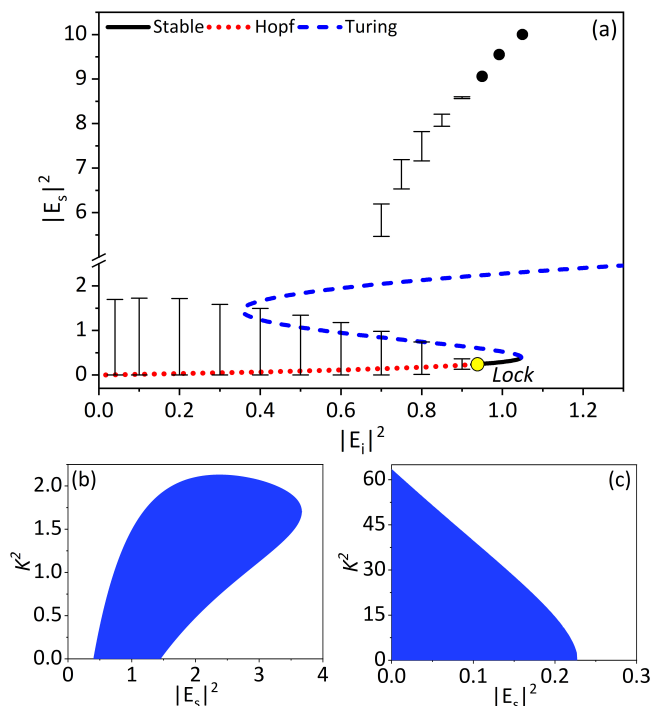
FIG. 1. (a) Steady state curve along with the unstable domains and the cavity soliton branch. Vertical bars show the time average of the maximum amplitude of the intensity oscillations due to Hopf. Injection locking point is depicted by a circle at the position $|E_i|^2_{IL} = 0.937$, $|E_s|^2_{IL} = 0.234$. (b) Turing and (c) Hopf instability domains in $|E_s|^2 - K^2$ plane. K corresponds to the frequency associated with the transverse mode whose wave vector has modulus K. Parameter values in the text.
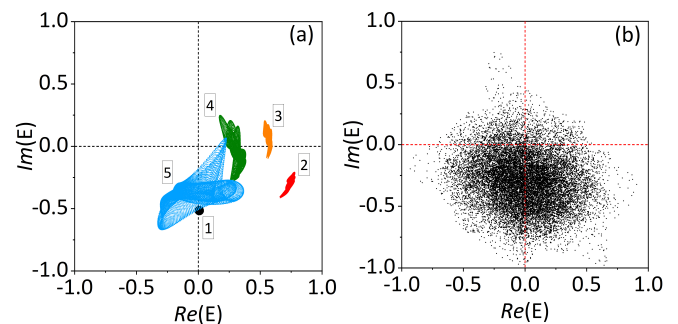

FIG. 2. Field distributions in the Argand plane as $Re(E)$ and $Im(E)$ in all the points of the grid at a fixed time. (a) Unlocked state at $|E_i|^2 = 0.46$ at $t = 0.84$ ns labeled 2 (red), at $t = 0.86$ ns labeled 3 (orange), at $t = 0.92$ ns labeled 4 (green), and at $t = 1.60$ ns labeled 5 (blue). (b) Fully unlocked state at $t = 6.4$ ns. The initial locked state at $|E_i|^2 = 0.95$ at $t = 0$ is shown in (a) labeled 1 (black circle).

We then turn our attention to CSs existing on top of the spatio-temporally chaotic background. We show that oscillating CSs due to the Hopf unstable background do not emit RWs while RWs are abundantly emitted by the surrounding background radiation via VMT. Such coexistence of CS and RW emitting VMT states constitutes the regimes of study in this paper. Despite the amplifying nature of CSs due the presence of excess gain, they inhibit instead of enhance the emission of extreme pulses that would otherwise be generated by the background emission in their absence. This observation is confirmed by the almost Gaussian distribution of total intensities collected in a finite area around the CS and its comparison with heavily tailed distribution of intensities in far areas from the CS tails which follows a negative exponential fit. We conclude that VMT remains the main source of RWs in lasers with optical injection even when CSs generate large peaks of the laser intensity.

In section 2 we introduce the model equations along with the homogeneous stationary solutions and the instabilities. In section 3 the statistical analysis concerning RW emission and its connection to nonlinear dynamical features of the Hopf domain is presented. In section 4 we introduce a regime where CSs can stably exist atop a RW emitting spatio-temporally chaotic background and show the ability of CSs to inhibit extreme events through statistical analyses and considerations regarding the formation of vortices. Finally, in section 5 we draw the conclusions and discuss the physical aspects of the connection between CSs, VMT and extreme events.

affected by a Hopf instability[29,32] or atop a spatially unstable background affected by a Turing instability[33]. The motivations of this paper are better served by the full set of Maxwell-Bloch equations rather than the reduced form since carrier diffusion and polarization dynamics, which act as spectral filters, play an important role in the complex dynamics below injection locking. For completeness, we compare simulation results of Maxwell-Bloch equations in the full and reduced forms, with and without the transverse carrier diffusion. We show that the macroscopic polarization variable, which is absent in the reduced form of the equations, provides the most important spectral filter effect when studying the spatiotemporal chaotic states.

Here we study the nonlinear dynamics of the Hopf unstable domain while considering the injection intensity as the control parameter. In these regimes we investigate the interplay of VMT and CSs on the onset of extreme events in semiconductor lasers with injection. The reason to do this is that in lasers with saturable absorbers the set of parameters more suitable for finding extreme events is compatible with that of stationary and oscillating CSs[16]. Would this apply to the case of optical injection too? We show first that the expansion of the limit cycle orbits away from the injection locking point (lower injection intensities) has direct consequences on the formation of the RWs at the peaks of spatio-temporally chaotic structures.

II. MODEL EQUATIONS

The following complete set of Maxwell-Bloch equations can suitably describe an injected broad-area VCSEL[28–32]:

$$\partial_t E = \sigma[E_i + P - (1 + i\theta)E + i\nabla^2_\perp E], \tag{1}$$

$$\partial_t P = \xi(D)[(1 - i\alpha)f(D)E - P], \tag{2}$$

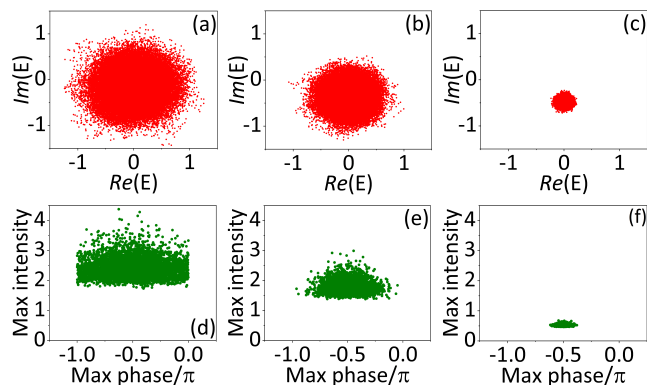$$\partial_t D = \mu - D - 1/2(EP^* + E^*P) + d\nabla^2_\perp D, \tag{3}$$

FIG. 3. Top row: field distributions in the Argand plane of the unstable Hopf background. Bottom row: intensity versus phase values of the maximum points. (a,d) $|E_i|^2 = 0.1$, (b,e) $|E_i|^2 = 0.5$, and (c,f) $|E_i|^2 = 0.9$.
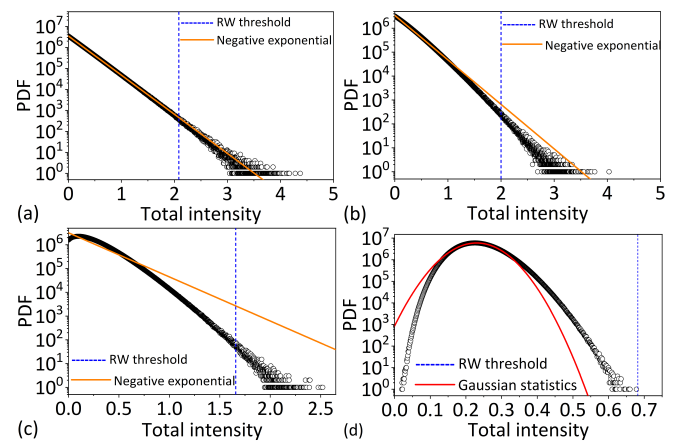

FIG. 4. Probability density functions (PDF) of all the intensity values: (a) $|E_i|^2 = 0.1$, (b) $|E_i|^2 = 0.3$, (c) $|E_i|^2 = 0.6$ and (d) $|E_i|^2 = 0.9$. Data acquisition time is 20 ns for all.

where E and P are the slowly varying amplitudes of the electric field and the macroscopic semiconductor polarization variables, respectively, D is the carrier density, σ is the photon decay rate, E_i is the amplitude of the external injection, θ is the frequency detuning between cavity and optical injection, α is the linewidth enhancement factor, μ is the pump parameter, and d is the carrier diffusion constant. Diffraction is described by the transverse Laplacian operator, $\nabla_\perp^2$, and the spatial variables are scaled to the square root of the diffraction parameter (typically of the order of $4\check{}5\mu m$). Time is scaled to the carrier decay time, which is assumed to be 1 ns. For a photon lifetime in the cavity of about 2.5 ps, the photon decay rate is $\sigma = 400$.

The function $f(D) = D - \beta D^2$ accounts for a nonlinear dependence of gain on carrier density and the value of $\beta = 0.125$ that we use here is obtained as the best fit of the gain calculated with the microscopic model[34]. The complex function $\xi(D)$ provides a phenomenological description of the susceptibility of the semiconductor material defined as

$$\xi(D) = \Gamma(D)(1 - i\alpha) + 2i\varepsilon(D), \quad (4)$$

where $\Gamma(D)$ is associated with the width of the gain curve and $\varepsilon(D)$ represents the detuning between the reference frequency and the peak of the gain curve provided that $|\varepsilon(D)| \ll \Gamma(D)$. The dependence of Γ and ε on D takes into account the changes of the susceptibility as the carrier density varies. In this paper, we set $\Gamma(D) = (0.560D + 0.293) \times 10^4$ and $\varepsilon(D) = (0.155D + 0.054) \times 10^4$. The other parameters are $\alpha = 4$, $\theta = -2$, and $d = 0.052$ unless stated otherwise.

For comparison, we also introduce a reduced form of Eq. (1-3) where the polarization of the semiconductor medium has been adiabatically eliminated. However, to retain the role of the macroscopic polarization P as a spectral filter and to avoid unphysical short wavelength instabilities below the injection locking point, a diffusive term δ is phenomenologically introduced in the equation for the electric field. The existence of a most unstable wave-vector and of a finite band of unstable wave-vectors cannot be reproduced after the standard adiabatic elimination of P from the full set of Maxwell-Bloch equations (1-3) since it amounts to assuming infinite width of the gain leading to the wrong prediction that all the wave-vectors K are equally unstable below the injection locking point. The effect of the diffusion term is that of adding a damping term $-\sigma\delta K^2 E_K$ to any transverse mode E_K with transverse wave vector of modulus K. The diffusion term can therefore also be interpreted as a loss term for modes that propagate in an oblique direction in a transversely finite cavity.

The value of the diffusion term $\delta = 0.01$ was chosen as the smallest possible value to avoid self-collapsing and will take into account a finite linewidth for the laser gain[25]. A detailed derivation can be found in[35] for a two-level system and in[36] for both a two-level system and a VCSEL. Such a reduced form is given as

$$\partial_t E = \sigma[E_i - (1 + i\theta)E + (1 - i\alpha)f(D)E$$
$$+ (\delta + i)\nabla_\perp^2 E], \quad (5)$$
$$\partial_t D = \mu - D - |E|^2 f(D) + d\nabla_\perp^2 D. \quad (6)$$

These sets of dynamical equations, Eq. (1-3) and Eq. (5,6), were numerically integrated by a split-step programming method with periodic boundary conditions. We have used space step of 0.5 for a box of size 256×256 which corresponds to spatial size of $512 \times 512\mu$ m for the device and space unit of 2 μ m for our simulations.

A. Homogeneous stationary solutions and instabilities

The dynamical equations (1-3) as well as (5,6) admit a plane wave stationary solution $E = E_s$, $P = P_s$, $D = D_s$ by setting $\partial_t = 0$, $\nabla_\perp^2 = 0$. The equation that links the output intensity $|E_s|^2$ to the input intensity $|E_i|^2$ is given by

$$|E_i|^2 = |E_s|^2[(1 - D_s + \beta D_s^2)^2 + (\theta + \alpha D_s - \alpha\beta D_s^2)^2], \quad (7)$$
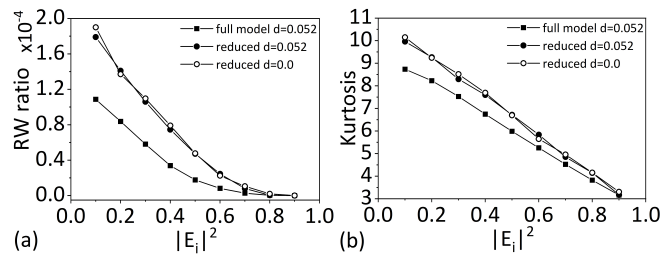
FIG. 5. (a) RW ratio and (b) kurtosis values versus the injection intensity. Data acquisition time as in Fig. 4.

where

$$D_s = \frac{1 + |E_s|^2 - \sqrt{(1 + |E_s|^2)^2 - 4|E_s|^2 \beta \mu}}{2|E_s|^2 \beta}. \tag{8}$$

The stationary curve can be bistable depending on the parameters μ, α, and θ. The nonlinear gain coefficient β is also an important parameter that modifies both the shape of the stationary curve and laser threshold condition. In order to determine the threshold value μ_{th} in absence of the injected field (free running laser) and in the plane-wave approximation, we must set $E_i = 0$ and $\theta = -\alpha$ in Eq. 7. This implies either $E_s = 0$ or $1 - D_s + \beta D_s^2 = 0$. The latter equation combined with Eq. 8 provides an equation which links the stationary intensity $|E_s|^2$ with the pump μ. At threshold $|E_s|^2 = 0$ and Eq. 8 gives $D_s = \mu$. Replacing D_s with μ in the equation $1 - D_s + \beta D_s^2 = 0$ we obtain the threshold value:

$$\mu_{th} = \frac{1 - \sqrt{1 - 4\beta}}{2\beta}. \tag{9}$$

For the case of this paper that considers nonlinear gain $\beta = 0.125$, the laser threshold is $\mu_{th} = 1.171$ and we study the regime of $\mu = 1.2\mu_{th}$ which corresponds to $\mu = 1.406$. The parameter values chosen in this paper guarantee an S-shaped form of the stationary curve as shown in Fig. 1(a). The chosen value of the pump current which is much lower than that in[25] is necessary to have the injection locking point on the lower HSS branch and a region where the background for the CSs is stable. We shall discuss the details in the following sections.

The stability of the homogeneous solutions is analyzed by studying the response of the system against perturbations of the form $\Delta \Xi \exp(\lambda t + i\mathbf{K} \cdot \mathbf{r})$, with $\Xi = E, P, D$ and λ is the growth rate of the perturbation. Two types of instability can now be obtained: (i) the Turing instability (Re$\lambda > 0$ and Im$\lambda = 0$) which affects the negative slope branch ($K = 0$) and part of the upper branch, does not depend on ξ hence independent of the way we describe the semiconductor susceptibility, only slightly affected by the pump current, and is responsible for the formation of patterns and eventually CSs[37]; (ii) the Hopf instability (Re$\lambda > 0$ and Im$\lambda \neq 0$) which is associated with lasers with an injected signal and appears whenever the frequency of the injected field differs from that of the free running laser. Such bifurcation is affected substantially by the pump current, exists for low injection intensities, and disappears at the injection locking point where the injec-
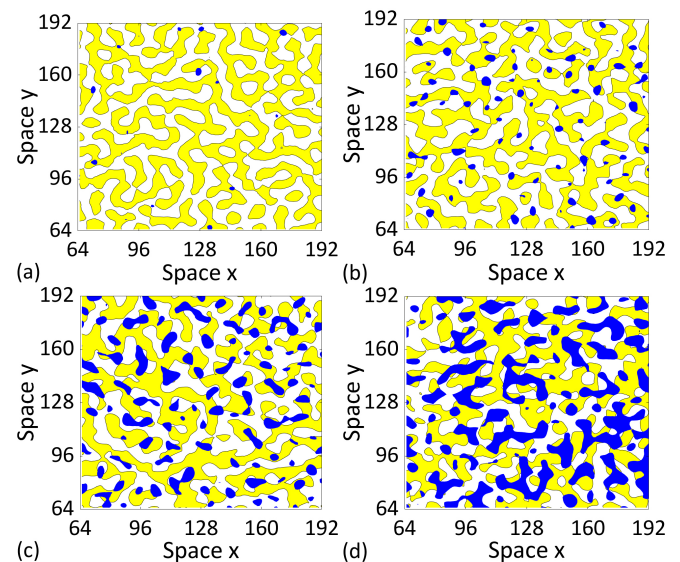

FIG. 6. Optical vortices in the contour plot of the real (yellow and light) and imaginary (blue and dark) parts of the electric field. (a) $|E_i|^2 = 0.7$, (b) $|E_i|^2 = 0.5$, (c) $|E_i|^2 = 0.3$ and (d) $|E_i|^2 = 0.1$.

tion intensity is large enough to lock the laser to its own frequency. The coordinates of the injection locking point are $|E_i|^2_{IL} = (\theta + \alpha)^2(\mu - \mu_{th})$ and $|E_s|^2_{IL} = \mu - \mu_{th}$. With our choice of the parameters $|E_i|^2_{IL} = 0.937$ and $|E_s|^2_{IL} = 0.234$. These two instability domains are shown in Fig. 1(b-c) and were also mapped on the steady state curve in Fig. 1(a).

B. Nonlinear dynamics in the Hopf instability domain

In Fig. 2, we show how the Hopf instability sets in when the control parameter (injection intensity) is decreased from a locked state to an unlocked state. It is seen from Fig. 2(a) that starting from an injection locked solution at time zero (the black circle labeled 1) and by switching the value of $|E_i|^2$ to 0.46 inside the Hopf unstable domain, the system first moves along its phase degree of freedom, see labels 2, 3 and 4, and then excites an amplitude instability (see the one labeled 5) in a way similar to what seen in[9,26]. Finally, a regime of extended spatio-temporal chaos is reached where amplitude and phase instabilities invade the entire transverse structure, see Fig. 2(b). VMT is expected here.

In Fig. 3(a-c) we look at the field distributions in the Argand plane of the unstable Hopf domain for different injection intensities. In these figures, one moves from a completely phase and amplitude unbound solution, Fig. 3(a) for $|E_i|^2 = 0.1$, to an almost bound solution just before the injection locking point, Fig. 3(c) for $|E_i|^2 = 0.9$. In Fig. 3(d-f) the same transition is shown plotting intensity versus phase values of the points where the intensity has a maximum. These observations imply that the unbound state, which corresponds to spatiotemporal chaos of large oscillation amplitude, is enhanced by moving to lower injection values inside the Hopf domain. We will see in later sections that high amplitude spatiotempo-
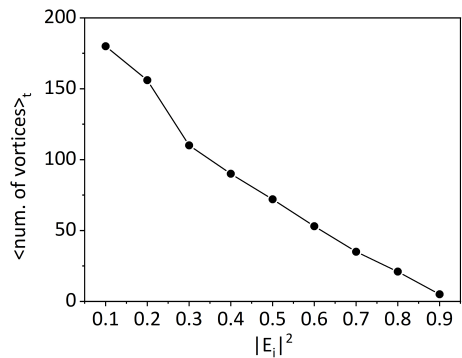
4

FIG. 7. Average number of vortices over time in the spatio-temporal chaotic regimes with increasing injection. Simulation time is 20ns.

ral chaos has direct consequences in the vortex density, and number and intensity of RWs.

III. ROGUE WAVES ANALYSIS

RWs corresponds to short-lived and large intensity peaks in a spatio-temporally chaotic state. They satisfy a widely accepted threshold defined for characterizing RWs, i.e. $\langle I \rangle + 8\sigma$, where σ is the standard deviation[9,15,16,21,25,38]. Moreover, the extremeness of events can be checked via the probability density function (PDF) of all the intensity values obtained during simulations. For the considered RW threshold, a positive deviation from a negative exponential function $\exp(-I/<I>)/<I>$ should be regarded as a signature of extreme events in the system[39]. Two other indicators are also used to measure the degree of rogueness, RW ratio and kurtosis[16] corresponding, respectively, to the number of spatio-temporal events with intensities exceeding the RW threshold to the total number of spatio-temporal events during simulation and to the ratio of the fourth moment about the mean to the square of the variance

$$\mathscr{K} = \frac{\frac{1}{n}\sum_{i=1}^{n}(I_i - \langle I \rangle)^4}{\left[\frac{1}{n}\sum_{i=1}^{n}(I_i - \langle I \rangle)^2\right]^2}. \qquad (10)$$

Roughly speaking, higher values of kurtosis correspond to larger positive deviation from the negative exponential associated with Gaussian statistics. In Fig. 4(a-d) we show the PDF of total intensity for different injection intensities. In correlation with the discussion of sec. II B, spatio-temporal events deviate the most from the negative exponential fit and exceed the most the RW threshold value when the device is operated far from injection locking point. Large intensity events approach normal distributions close to the injection locking point. Suppression of the chaoticity and thus strong reduction of the number of RWs by increasing the injection strength are well illustrated by RW ratio and kurtosis curves shown in Fig. 5.

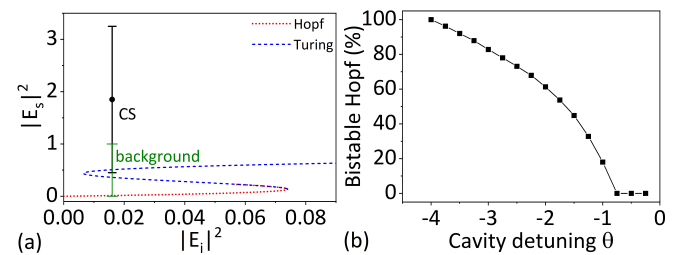The details of population, phase and gain dynamics at the

FIG. 8. (a) The steady state curve with the Turing and Hopf unstable domains for $\theta = -3.5$. The CS considered in our simulation is shown by a black circle at $|E_i|^2 = 0.016$. Note that the entire lower branch is Hopf unstable and the average value is used for the CS intensity. The black and green vertical bars show the average extent of intensity oscillations for the CS and the background respectively. (b) Variation of the extent of the Hopf region in the lower branch which is coexistent with the upper branch when varying θ. For $\theta = -4$ the entire Hopf branch coexists with an upper state.

time of RW formation are essentially the same as those discussed in[25] for the same system using a reduced model with no carrier transverse diffusion involved. In terms of RW statistics, however, we observe from Fig.5(a) and (b) that adiabatic elimination of the macroscopic polarization in the reduced equations (5,6) seems to be responsible for more chaotic states with larger number of RWs (by more than 40 percent) and kurtosis values (by more than 15 percent) while the inclusion of a diffusion factor for the electric field seems to be unable to fully reproduce the same spectral filter effect. We also observe that, unlike semiconductor lasers with saturable absorber where carrier diffusion plays a significant role in stabilizing or destabilizing a spatiotemporally chaotic state leading to either enhancement or suppression of extreme events depending on the ratio of carrier lifetimes in active and passive materials[24], here in the semiconductor laser with injection carrier diffusion plays a minor contribution.

It is useful now to look into the electric field phase behavior to establish a possible connection between VMT due to optical vortices and formation of RWs. Optical vortices (or photonic quantum vortices) are phase singularity points with zero intensity that has revealed interesting relations between macroscopic physical optics and microscopic quantum optics[40]. The zero-intensity point at the core of an optical vortex represents a point where the phase of the light field is not defined, i.e. a singularity. The integral of the gradient of the phase on a circular path around the singularity is plus or minus 2π (topological charge). This continuous change in phase results in spiral phase patterns around the singularity, which is a defining feature of the optical vortices. The topological features of phase defects ensure that the singularities are well-defined and robust to perturbations. VMT in lasers with injection and its relevance to RW formation is discussed in details in[9,26]. Here we focus on the abundance of such vortices for different injection intensities and conclude that the degree of chaoticity and thus the number of emitted RWs are correlated with the number of optical vortices in VMT. In Fig. 6 we show the contour plots for the real (light yellow) and imaginary (dark blue) parts of the electric field, where color-filled areas correspond
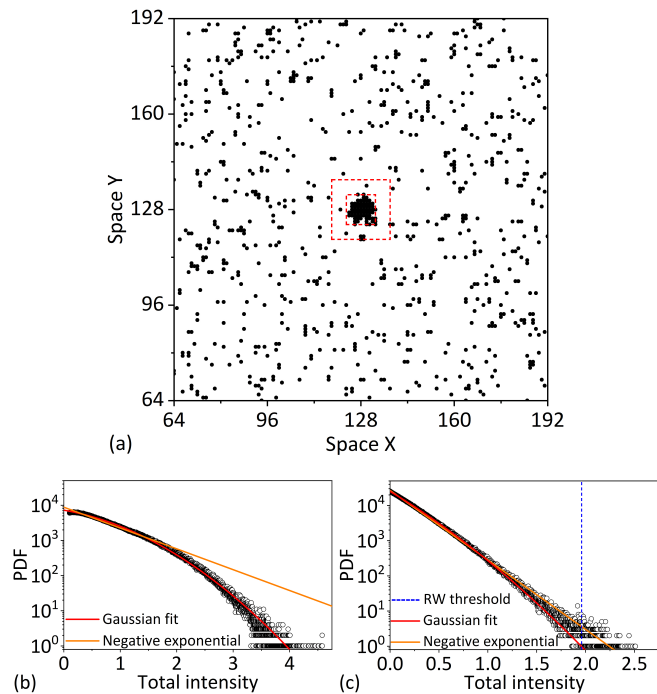
(a)

(b)

(c)

FIG. 9. (a) Spatio-temporal intensity maxima obtained for simulation window of 2 ns and square regions of data acquisition around the CS. The smaller box corresponds to the CS area bounded by its tails. The larger box extends from the tails of the CS up to 3 times the FWHM value of the CS (10 μm). PDF of all the intensity values obtained inside (b) the smaller square shown in (a) and (c) the larger square far from tails of the CS. We note that in (c) and similar analyses in the rest of the paper, CS intensities are excluded from the statistics of the background VMT state. Number of data points is 6050000 for both. Note that the RW threshold for (b) is 4.98.

to positive values for Re(E) and Im(E). The zero isolines for each variable are determined by the border of each area and every crossing between them corresponds to a zero in the output intensity corresponding to an optical vortex. The number of crossings between the zero isolines and thus the number of vortices increases by moving deeper inside the Hopf region away from the injection locking point, see Fig. 6(a-d). In Fig.7 the average number of vortices in the spatio-temporal chaotic regime is plotted with increasing injection which is obtained by determining the saturation point of the average number of intensity points with a larger value than a specific threshold. This provides quantitative evidence of increasing number of RWs with increasing number of vortices. This has to be expected when VMT is the mechanism underlying the appearance of RWs.

IV. CAVITY SOLITONS, VORTEX MEDIATED TURBULENCE AND EXTREME EVENTS

To study the dynamical behavior of CSs over a spatio-temporally chaotic background and its relevance to emission of RWs, we increase the absolute value of the cavity detuning to $\theta = -3.5$ in order to guarantee a bistability of a background
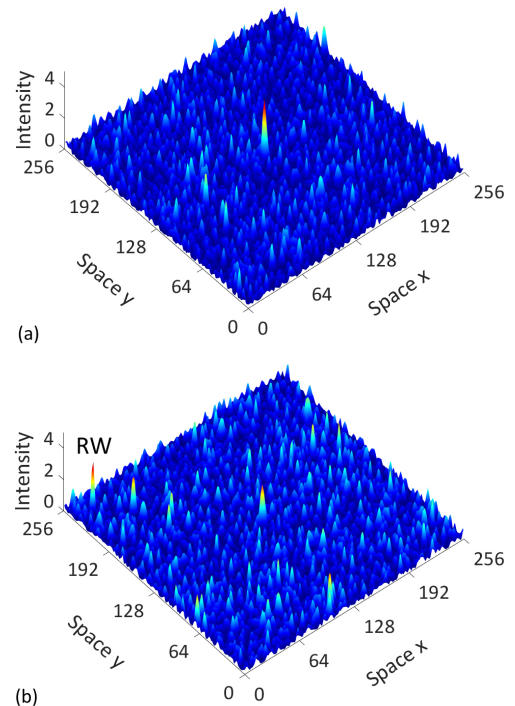

(a)

(b)

FIG. 10. (a) A CS excited at the center of the transverse section by an address pulse in absence of RWs. (b) Emission of a RW in presence of the CS at the center. RW intensity is larger than the CS intensity by 49 percent at this specific moment of RW emission.

with strong chaoticity and an upper branch where CSs can exist, see Fig. 8(a). Figure 8(b) shows instead the percentage of the lower Hopf unstable branch which becomes coexistent with the upper branch by increasing the absolute value of the cavity detuning. We observe that for $\theta = -\alpha = -4$ the entire Hopf unstable part of the lower branch coexists with an upper branch. Here, we focus on a single excited CS located at the center of the transverse domain and analyze the situation with no loss of generality. The chosen values of the parameters corresponds to CSs on a VMT background.

For the statistical analyses of the situation illustrated in Fig. 8(a), we introduce two different square regions around the CS excited at the center of a 256×256 box and collect all intensity values of each square separately, as shown in Fig.9(a) where the spatio-temporal maxima are depicted in a simulation that is long enough to guarantee almost the same number of data points. Simulations were run for a suitable time span to obtain equal number of data points for the two square areas as their sizes are different. We observe RWs to form at locations far from the CS tails, at least on the order of 3 times the FWHM value of the CS roughly equal to 10 μm. In Fig.9(b,c) we have shown the PDF of the square regions depicted in Fig.9(a) where Fig.9(b) confirms that spatio-temporal events do not deviate from the negative exponential function and thus no RWs are emitted at the location of the CS up to the end of its tails. Instead, we see from Fig.9(c) that in regions away from the CS tails, RWs due to VMT are abundant and we observe intensities deviating from the negative exponential fit
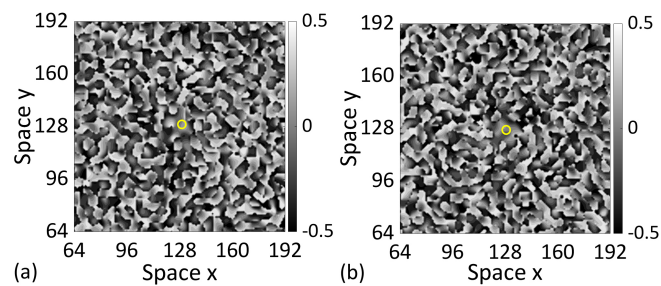
6

(a) (b)

FIG. 11. Snapshot of phase distributions of the electric field separated by 0.056 ns from each other. (a) corresponds to the situation shown in Fig. 10(b) at the time of a RW emission. Empty circles correspond to CSs.
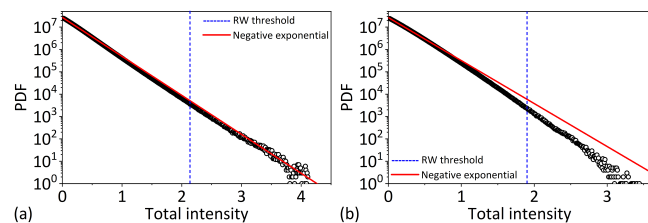

(a) (b)

FIG. 12. Total intensity PDF in the absence (a) and presence (b) of several CSs in random positions. The situation is shown in Fig.13 with 15 CSs. Parameter values as in Fig.9.
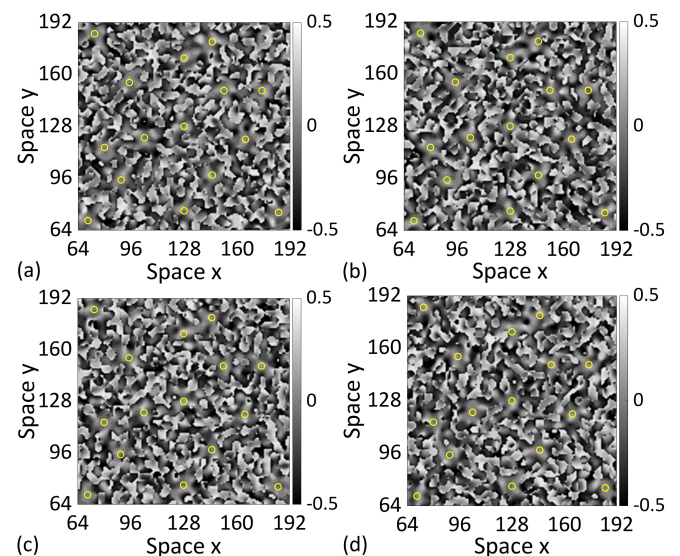

(a) (b)

(c) (d)

FIG. 13. Vortex clearing effect by 15 randomly positioned CSs in consecutive snapshots of the field phase moving forward in steps of 0.04 ns from (a) to (d). The CSs are depicted by empty circles. Parameter values as in Fig.9.
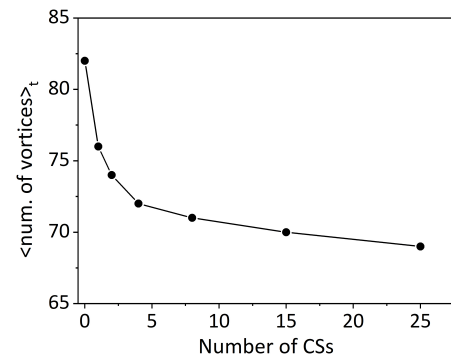

FIG. 14. Average number of vortices versus the number of CSs present in the output emission. Parameter values as in Fig.9.

with RW ratio of around 8×10^{-5}.

It is also interesting to note that in all instances during the spatio-temporal dynamics, the intensity of the RWs at the time of their emission is higher than the CS intensity at the same moment, as shown for example in Fig.10, although the maximum peak intensity of the CS can be larger than the RWs in its erratic oscillations at the times of no RW emission.

To further look into the issue, we plotted the phase distributions of the output field in the presence of a CS at two sequential times in Fig.11. We observe from Fig.11 that at the location of the CS and in a finite surrounding region the field phase tends to change smoothly and does not present singularities typical of vortices responsible for the formation of RWs. The absence of rapid phase changes in the CS location and its surrounding area corresponds to the absence of local vortices in the neighborhood of the CS. Without a compensating number of vortices arising in other parts of the transverse space, we conclude that the region occupied by a CS in lasers with coherent injection not only inhibits the creation of RWs locally but also does not enhance vortex density in other regions of the transverse plane. Thus, in absence of vortex clearing effects away from CS tails, we observe the unaltered background dynamics seen without CS with generation of RWs via VMT.

Since the formation and annihilation of optical vortices accompanied by abrupt changes of the field phase are key ingredients for VMT leading to the emission of RWs in lasers with coherent injection[9,26], CSs inhibit spatio-temporal rare events. A more effective inhibition action could be obtained if more than one CS is switched on. In[28] it was shown that in the presence of an unstable background, CSs can interact even at

very large distances. Therefore, one would expect that with a relative small number of CSs in random positions, RWs can be suppressed everywhere. In Fig.12, we compare the PDF of the total intensity obtained in the same transverse area without and with CSs. The suppression of RWs in the entire area due to the presence of 15 randomly positioned CSs is clear as all the intensity points are below the negative exponential fit in Fig.12(b). Extended vortex clearing effect by 15 randomly positioned CSs can be observed in the consecutive snapshots of Fig.13 where crossing of zero isolines is rare. More notable in these figures is the absolute absence of vortices along the lines connecting closer CSs. Reduction of vortices by the presence of CSs is shown in Fig.14 where the number of CSs is progressively increased from zero (no CS in the output emission) to larger numbers for which the reduction in the average number of vortices tends to saturate.

7

V. CONCLUSION

We investigated broad-area semiconductor lasers like e.g. VCSELs, with coherent injection to identify the key mechanisms for the generation of rogue waves in the region of Hopf instability. We first discuss that the degree of spatio-temporal chaos in the Hopf domain depends on the distance from the injection locking point with direct consequences on the generation of RWs, their number and intensity. In agreement with[9,25,26], VMT has been identified as the mechanism behind the generation of RWs by checking the number of optical vortices found at the crossing points of zero isolines of the real and imaginary pars of the the electric field. We measured that the number of optical vortices decreases when approaching the injection locking point and then found a region of co-existence of VMT and CSs. This gave us the possibility of addressing the question how CS emission may influence RW generation[16]. We found instead that CSs excited on spatio-temporally chaotic backgrounds of lasers with injection have an inhibition effect on RW generation. Since the core of optical vortices requires the local intensity to be zero, it is not surprising that close to the maximum intensity of CSs no vortices are detected. What is unexpected is that the presence of a CS forbids the formation of optical vortices in areas surrounding their tails and does not promote increasing vortex densities in areas away from their peaks. These effects lead to a normal distribution of events and inhibit the occurrence of extreme events. The reason lies in the fact that the presence of a CS in lasers with coherent injection maintains smooth field phase changes in its vicinity leading to clearance of local vortices around the CS. As the creation and annihilation of optical vortices with abrupt phase changes are essential for the generation of RWs in such lasers, CSs act as inhibitors of spatio-temporal rare events. Extensive clearing of vortices and RWs by several randomly positioned CSs was also demonstrated as a consequence of long range interactions of CSs. We note that away from the tails of the CSs, RW generation via VMT remains unchanged leading to sudden local peaks with intensities higher than that of the CSs. The new inhibition effect of CSs in dissipative systems displaying VMT can be used to locally control the emission of RWs with useful applications in modern imaging and sensing platforms[19].

DATA AVAILABILITY STATEMENT

The data that support the findings of this study are available from the corresponding author upon reasonable request.

[1] D. R. Solli, C. Ropers, P. Koonath, and B. Jalali, Nature **450**, 1054 (2007).
[2] N. Akhmediev and E. Pelinovsky, Eur. Phys. J. Spec. Top. **185**, 1 (2010).
[3] C. Bonatto, M. Feyereisen, S. Barland, M. Giudici, C. Masoller, J. R. Rios Leite, and J. R. Tredicce, Phys. Rev. Lett. **107**, 053901 (2011)
[4] M. Onorato, S. Residori, U. Bortolozzo, A. Montina, and F. T. Arecchi, Physics Reports **528**, 47 (2013).
[5] J. M. Dudley, F. Dias, M. Erkintalo, and G. Genty, Nature Photonics **8**, 755 (2014).
[6] N. Akhmediev et al., J. Opt. (Bristol, U.K.) **18**, 063001 (2016).
[7] L. Gao, Q. Wu, Y. Cao, S. Wabnitz, and T. Zhu, J. Phys. Photonics **2**, 032004 (2020).
[8] P. Coullet, L. Gil, and J. Lega, Phys. Rev. Lett. **62**, 1619 (1989).
[9] C. Gibson, A. M. Yao, and G.-L. Oppo, Phys. Rev. Lett. **116**, 43903 (2016).
[10] M. G. Clerc, G. Gonzalez-Cortes, and M. Wilson, Optics Letters **41**, 2711 (2016).
[11] F. Selmi, S. Coulibaly, Z. Loghmari, I. Sagnes, G. Beaudoin, M. G. Clerc, and S. Barbay, Physical Review Letters **116**, 013901 (2016).
[12] S. Coulibaly, M. G. Clerc, F. Selmi, and S. Barbay, Physical Review A **95**, 023816 (2017).
[13] M. Tlidi and K. Panajotov, Chaos **27**, 013119 (2017).
[14] K. Panajotov, M. G. Clerc, and M. Tlidi, Eur. Phys. J. D **71**, 176 (2017).
[15] M. Eslami, M. Khanmohammadi, R. Kheradmand, and G.-L. Oppo, Phys. Rev. A **96**, 033836 (2017).
[16] C. Rimoldi, S. Barland, F. Prati, and G. Tissoni, Physical Review A **95**, 023841 (2017).
[17] S. Perrone, R. Vilaseca, J. Zamora-Munt, and C. Masoller, Physical Review A **89**, 033804 (2014).
[18] D. Pierangeli, G. Musarra, F. Di Mei, G. Di Domenico, A. J. Agranat, C. Conti, and E. DelRe, Phys. Rev. A **94**, 063833 (2016).
[19] T. Jin, Ch. Siyu, and C. Masoller, Optics Express **25**, 31326 (2017).
[20] K. Panajotov, M. Tlidi, Y. Song, and H. Zhang, Chaos **30**, 053103 (2020).
[21] K. Talouneh, C. Rimoldi, R. Kheradmand, G. Tissoni, and M. Eslami, Physical Review A **102**, 033508 (2020).
[22] H. Li and K. Iga, Vertical-Cavity Surface-Emitting Laser Devices, Springer Series in Photonics, (2003).
[23] R. Michalzik, VCSELs: fundamentals, technology and applications of vertical-cavity surface-emitting lasers, Springer Series in Optical Sciences, vol. 166. Berlin, Germany (2013).
[24] K. Talouneh, R. Kheradmand, G. Tissoni, and M. Eslami, Physical Review A **105**, 013501 (2022).
[25] C. Rimoldi, M. Eslami, F. Prati, and G. Tissoni, Physical Review A **105**, 023525 (2022).
[26] G.-L. Oppo, Chaos, Solitons & Fractals **155**, 111750 (2022).
[27] G.-L. Oppo, G.-L. Lippi, A. Politi, and F. T. Arecchi, Phys. Rev. A **34**, 4000 (1986).
[28] Sh. R. Anbardan, C. Rimoldi, R. Kheradmand, G. Tissoni, and F. Prati, Physical Review E **101**, 042210 (2020).
[29] X. Hachair, F. Pedaci, E. Caboche, S. Barland, M. Giudici, J. R. Tredicce, F. Prati, G. Tissoni, R. Kheradmand, L. A. Lugiato, I. Protsenko, and M. Brambilla, IEEE Journal on Selected Topics in Quantum Electronics **12**, 339 (2006).
[30] C. McIntyre, A. M. Yao, G.-L. Oppo, F. Prati, and G. Tissoni, Phys. Rev. A **81**, 013838 (2010).
[31] F. Prati, G. Tissoni, C. McIntyre, and G.-L. Oppo, Eur. Phys. J. D **59**, 139 (2010).
[32] M. Eslami, R. Kheradmand, and K. M. Aghdami, Physica Scripta **T157**, 014038 (2013).
[33] M. Eslami and G.-L. Oppo, European Physical Journal D **75**, 125 (2021).
[34] M. Eslami, R. Kheradmand, Gh. Hashemvand, Optical and Quantum Electronics **46**, 319 (2014).
[35] S. V. Fedorov, A. G. Vladimirov, G. V. Khodova, and N. N. Rosanov, Phys. Rev. E **61**, 5814 (2000).
[36] G. L. Oppo, A. M. Yao, F. Prati, and G. J. deValcárcel, Phys. Rev. A **79**, 033824 (2009).
[37] W. J. Firth and A. J. Scroggie, Phys. Rev. Lett. **76**, 1623 (1996).
[38] G.-L. Oppo, A. M. Yao, and D. Cuozzo, Phys. Rev. A **88**, 043813 (2013).
[39] M. Onorato, S. Residori, U. Bortolozzo, A. Montina, and F. T. Arecchi, Physics Reports **528**, 47 (2013).
[40] Y. Shen, X. Wang, Z. Xie, Ch. Min, X. Fu, Q. Liu, M. Gong, and X. Yuan, Light Sci. Appl. **8**, 90 (2019).